Journal of Materials Chemistry A

Accepted Manuscript

ROYAL SOCIETY OF CHEMISTRY

www.rsc.org/materialsA

Cite this: DOI: 10.1039/c0xx00000x

www.rsc.org/xxxxxx

ARTICLE TYPE

Hybridization of graphene nanosheets and carbon-coated hollow Fe_3O_4 nanoparticles as a high-performance anode material for lithium-ion batteries

Yongtao Zuo[a], Gang Wang[a*], Jun Peng[a], Gang Li[a], Yanqing Ma[a,*], Feng Yu[a], Bin Dai[a], Xuhong Guo[a,b], Ching-Ping Wong[c,d]

Received (in XXX, XXX) Xth XXXXXXXXX 20XX, Accepted Xth XXXXXXXXX 20XX
DOI: 10.1039/b000000x

Fe_3O_4 has long been regarded as a promising anode material for lithium ion battery due to its high theoretical capacity, earth abundance, low cost, and nontoxic properties. At present, no effective method has been realized to overcome the bottleneck of poor cyclability and low rate capability because of its huge volume change and low electrical conductivity. In this article, a facile synthesis strategy is developed to fabricate two-dimensional (2D) carbon encapsulated hollow Fe_3O_4 nanoparticles (H-Fe_3O_4 NPs) homogeneously anchored on graphene nanosheets (designated as H-Fe_3O_4@C/GNS nanosheets) as a durable high-rate lithium ion battery anode material. In the constructed architecture, the thin carbon shells can avoid the direct exposure of encapsulated H-Fe_3O_4 NPs to the electrolyte and preserve the structural and interfacial stabilization of H-Fe_3O_4 NPs. Meanwhile, the flexible and conductive GNS nanosheets and carbon shells can accommodate the mechanical stress induced by the volume change of H-Fe_3O_4 NPs as well as inhibit the aggregation of Fe_3O_4 NPs and thus maintain the structural and electrical integrity of the H-Fe_3O_4@C/GNS electrode during the lithiation/delithiation processes. As a result, the H-Fe_3O_4@C/GNS electrode exhibits outstanding reversible capacity (870.4 mAh g^{-1} at the rate of 0.1C (1 C = 1 A g^{-1}) after 100 cycles) and excellent rate performance (745, 445, and 285 mAh g^{-1} at 1, 5, and 10 C, respectively) for lithium storage. More importantly, the H-Fe_3O_4@C/GNS electrode demonstrates prolonged cycling stability even at high charge/discharge rates (only 6.8% capacity loss after 200 cycles at a high rate of 10 C). Our results show that the 2D H-Fe_3O_4@C/GNS nanosheets are promising anode materials for the next generation LIBs with high energy and power density.

[a] *School of Chemistry and Chemical Engineering, Key Laboratory of Materials-Oriented Chemical Engineering of Xinjiang Uygur Autonomous Region, Shihezi University, Shihezi, P.R. China. Email:gwangshzu@163.com, mayanqing@shzu.edu.cn*
[b] *State Key Laboratory of Chemical Engineering, East China University of Science and Technology, Shanghai 200237, P. R. China*
[c] *Department of Electronic Engineering, The Chinese University of Hong Kong, Shatin, NewTerritories, HongKong, SAR, China*
[d] *School of Materials Science and Engineering, Georgia Institute of Technology, Atlanta, GA, 30332, United States*

Cite this: DOI: 10.1039/c0xx00000x

www.rsc.org/xxxxxx

ARTICLE TYPE

1. Introduction

Rechargeable Li-ion batteries (LIBs) are now considered as the most important power sources for electric vehicles (EVs) and hybrid electronic vehicles (HEVs). In order to meet the increasing requirements for EVs and HEVs applications, lithium-ion batteries with larger energy density, higher power density, and longer cycle life are highly desirable.[1,2] However, the relatively low storage capacity (372mAh g^{-1}) of commercially used graphite anode still restricts its application in LIBs with high energy and power density. Therefore, much research interests have been prompted to focus on the research of new anode materials with superior capacity for LIBs, such as Si,[3] Sn[4] and other transition metal oxides.[5-7] Among various potential transition metal oxide anode materials, Fe_3O_4 shows high theoretical capacity (926 mAh g^{-1}), low cost, eco-friendliness, and natural abundance, thus has attracted considerable attention.[7,8] However, its severe volume expansions occurring upon Li^+ insertion and extraction causes the agglomeration of active materials, electrode pulverization and finally loss of electric contact with the current collector, thereby leading to poor cycling performance.[9] In addition, the low electrical conductivity of pristine Fe_3O_4 challenges the achievement of high capacity at high charge/discharge rates.[5]

In order to circumvent the above intractable problems, a variety of appealing strategies have been developed, including the nanostructured Fe_3O_4 materials with various morphologies, such as nanocapsules,[10] hollow beads,[11] wires,[12] arrays,[13] and nanocubes,[14] and various Fe_3O_4/carbon hybrids such as Fe_3O_4 nanoparticles embedded in a mesoporous carbon foam,[15-17] carbon-coated Fe_3O_4 nanostructures,[7,18,19] two-dimensional (2D) graphene/Fe_3O_4,[20-46] or carbon nanosheets/Fe_3O_4 hybrids.[47,48] In particular, the composites of graphene and Fe_3O_4 have been reported to have high capacity and excellent cycling performance. For examples, Sun and coworkers[20] reported a vacuum filtration and thermal reduction processes to synthesize flexible free-standing hollow Fe_3O_4/graphene films, which exhibited a capacity of 940 mAh g^{-1} at 200 mA g^{-1} after 50 cycles. Cheng et al.[22] synthesized a flexible interleaved Fe_3O_4/graphene composite and obtained a reversible specific capacity of 1026 mAh g^{-1} at 35 mA g^{-1}. Xue and coworkers[24] reported the synthesis of a novel hollow porous Fe_3O_4 bead–rGO composite structure, which exhibited a reversible capacity of 1039 mAh g^{-1} after 170 cycles at a current density of 100 mA g^{-1}. However, the high rate performance of these materials highly needed for HEVs and EVs is still not satisfying. It may be attributed to the lack of favorable electronic and ion conductivity and the continuous growth of the unstable SEI films at the Fe_3O_4/electrolyte interface during cycling. Therefore, a novel design for the structure of the Fe_3O_4-based anode is highly needed to achieve both longer cycling life and higher rate performance.

Herein, we develop a facile synthesis strategy to fabricate 2D carbon-encapsulated hollow Fe_3O_4 nanoparticles homogeneously anchored on graphene nanosheets (designated as H-Fe_3O_4@C/GNS nanosheets) with excellent cycling stability and super high rate performance. As illustrated in Scheme 1, the overall synthetic procedure of H-Fe_3O_4@C/GNS nanosheets involves two steps. First, the hollow Fe_3O_4 nanoparticles/graphene nanosheets (H-Fe_3O_4/GNS nanosheets) were synthesized via a facile, one-step solvothermal approach by the in situ conversion of $FeCl_3$ to Fe_3O_4 and simultaneous reduction of GO to graphene in DEG–EG (1:1) mixed solvent. Then, carbon shells were coated onto hollow Fe_3O_4 nanoparticles (H-Fe_3O_4 NPs) by dispersing the H-Fe_3O_4/GNS nanosheets in glucose aqueous solution for hydrothermal treatment. As a result, a novel 2D carbon-encapsulated nanostructure composed of H-Fe_3O_4@C/GNS nanosheets was obtained. In the unique 2D encapsulation architecture, the thin carbon shells can effectively avoid the direct exposure of encapsulated Fe_3O_4 to the electrolyte and preserve the structural and interfacial stabilization of Fe_3O_4 NPs. Meanwhile, the thin carbon shells and the flexible and conductive 2D graphene nanosheets can effectively accommodate the mechanical stress induced by the volume change of anchored H-Fe_3O_4 NPs as well as inhibit the aggregation of Fe_3O_4 NPs and thus maintain the structural and electrical integrity of the H-Fe_3O_4@C/GNS electrode during the charge and discharge processes. As a result, this novel 2D H-Fe_3O_4@C/GNS nanosheets electrode exhibits superior LIBs performance with large reversible capacity, high rate capability, and excellent cycling performance at high rates, which could be employed as excellent anode materials for high-performance LIBs.

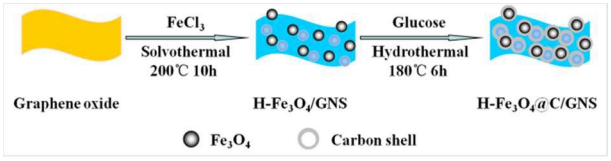

Scheme 1 Schematic representation of the fabrication process of H-Fe_3O_4@C/GNS nanosheets.

2. Experimental Section

2.1 Materials and methods

Natural graphite powder (325 mesh) was purchased from Alfa-Aesar and used without further purification. Iron (III) chloride hexahydrate ($FeCl_3 \cdot 6H_2O$, 98%), diethylene alcohol (DEG), ethylene alcohol (EG) was purchased from Adamas Reagent. Ethanol, sodium hydroxide, glucose, and anhydrous sodium acetate (NaOAc) were supplied by China Medicine Co. All the chemicals were of analytical grade and used without further purification.

Synthesis of H-Fe_3O_4/GNS nanosheets: The generation of H-Fe_3O_4/GNS nanosheets was carried out by a polyol-media solvothermal method. Typically, graphite oxide (0.5 g) prepared according to Hummers' method[49] was ultrasonicated in diethylene alcohol (DEG, 20mL) to produce a clear solution, and $FeCl_3 \cdot 6H_2O$ (1.35 g) was added with constant stirring for 30 min to form solution A. Then, polyethylene glycol (PEG-6000) (1.5 g)

and NaAC (3.6g) were dissolved in ethylene glycol (EG, 20 mL) to produce a clear solution B. After that, solution A and solution B were mixed and further ultrasonicated for 30 min. The mixed solution was subsequently transferred into a Teflon-lined stainless steel autoclave of 50 mL capacity and maintained at 200 °C for 20 h. After cooling to ambient temperature, the as-prepared H-Fe_3O_4/GNS nanosheets were collected by repeatedly washing with ethanol and water, followed by drying under vacuum at 80 °C for 12 h. The resulting powder was loaded into a tube furnace and heated under an argon gas atmosphere from room temperature to 500 °C at a heating rate of 10 °C min^{-1}, maintaining at this temperature for 3 h to obtain well-crystalline H-Fe_3O_4/GNS nanosheets.

Synthesis of H-Fe_3O_4@C/GNS nanosheets: H-Fe_3O_4@C/GNS nanosheets were prepared by a hydrothermal method. Typically, 2.5 mg mL^{-1} H-Fe_3O_4/GNS nanosheets were dispersed in 80 mL of 0.05 mol L^{-1} aqueous glucose solution. The mixture was then transferred into a Teflon-lined stainless steel autoclave with a capacity of 100 mL for hydrothermal treatment at 180°C for 6 h. After the reaction, the autoclave was cooled naturally to room temperature, and the suspensions were isolated by a magnet, washed with water and ethanol several times, and vacuum dried in an oven at 100°C for 12 h.

2.2. Material characterization

X-ray diffraction (XRD) of the samples was measured on a Bruker AXS D8 X-ray diffract meter with a Cu-Ka X-ray source operating at 40 kV and 100 mA. The morphologies of the samples were observed using scanning electron microscope (SEM, JEOL JSM-6490LV) and a transmission electron microscope (TEM, FEI Tecnai G2). Thermogravimetry analysis (TGA) was carried out on a simultaneous thermal analyzer (NETZSCH STA 449 F3) in an air atmosphere from room temperature to 700 ℃ at a rate of 10℃ min^{-1}. X-ray photoelectron spectroscopic (XPS) measurement was made on a PHI1600 ESCA system.

2.3. Electrochemical characterization

The electrochemical experiments were performed using 2032-type coin cells, with metallic lithium foil served as the counter electrode. The working electrodes were prepared with active materials, carbon black, and PVDF binder at a weight ratio of 8:1:1 in N-methyl-2 pyrrolidinone (NMP). The obtained slurry was coated onto Cu foil and dried at 120℃ for 12h. The dried tape was then punched into round plates with diameter of 12.0 mm as the cathode electrodes. The loading density of the electrode was about 2 mg cm^{-2}. The working electrode and counter electrode were separated by a Celgard 2400 membrane. The electrolyte used was 1 M LiPF6 dissolved in the mixture of ethyl carbonate (EC), dimethyl carbonate (DMC) and ethylmethyl carbonate (EMC) with the volume ratio of 1:1:1. The assembly of the cell was conducted in an Ar-filled glove box (H_2O and O_2<1ppm) followed by an overnight aging treatment before the test. Galvonostatic charge–discharge was measured on a LAND battery tester (LAND CT 2001A, China) in the voltage window of 0.005-3.0 V versus Li^+/Li. All of the specific capacities here were calculated on the basis of the total weight of active materials. Cyclic voltammetry (CV) and electrochemical impedance spectroscopy (EIS) were measured using a potentiostat (CHI 604C, CH Instrumental Inc.). The impedance spectra were carried out in the frequency range from 100 kHz to 0.01Hz.

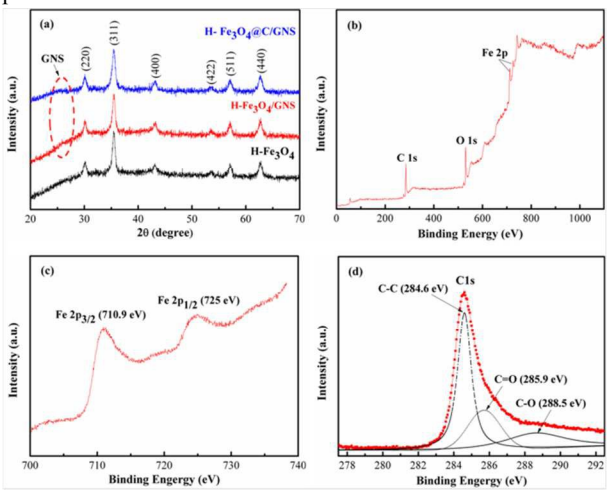

Figure 1 (a) XRD patterns of H-Fe_3O_4 NPs, H-Fe_3O_4/GNS nanosheets and H-Fe_3O_4@C/GNS nanosheets; (b) XPS spectra of H-Fe_3O_4/GNS nanosheets; (c) Fe 2p spectra of the H-Fe_3O_4/GNS nanosheets and (d) C 1s spectra of the H-Fe_3O_4/GNS nanosheets.

3. Results and discussion

The structure and composition of the samples are studied by X-ray diffraction (XRD), and X-ray photoelectron spectroscopy (XPS) analysis. Figure 1a shows the XRD pattern of the as-obtained H-Fe_3O_4 NPs, H-Fe_3O_4/GNS nanosheets and H-Fe_3O_4@C/GNS nanosheets. The diffraction peaks for three samples at 30.0 (220), 35.2 (311), 42.9 (400), 56.9 (511) and 62.5 (440) are consistent with the standard XRD data for the cubic phase Fe_3O_4 (JCPDS card, file no. 89-4319) with a face-centered cubic (fcc) structure. Besides these peaks, an additional peak at 24.8 corresponding to the graphene can be seen in the diffraction pattern of the H-Fe_3O_4/GNS nanosheets, indicating the coexistence of Fe_3O_4 and graphene in the nanosheets. The diffraction pattern of the H-Fe_3O_4@C/GNS nanosheets shows a similar trace to the H-Fe_3O_4/GNS nanosheets and no obvious sharp diffraction peak for the graphite is observed, confirming that the carbon shell prepared by this method is amorphous. Thermogravimetric analysis of H-Fe_3O_4/GNS nanosheets and H-Fe_3O_4@C/GNS nanosheets (Supporting Information, Figure S1) revealed that the weight fraction of Fe_3O_4 in the nanosheets was 85.0% and 79.9%, respectively, according to the remaining weight of Fe_2O_3.

Figure 1b shows the XPS survey spectrum of the H-Fe_3O_4/GNS nanosheets in the region of 0-1100 eV. The spectrum indicated the presence of carbon, oxygen, and iron, arising from H-Fe_3O_4 NPs and GNS. The Fe 2p XPS results (Figure 2c) show typical characteristics of Fe_3O_4 with two peaks located at 710.9 and 724.2 eV, corresponding to the Fe 2p3/2 and 2p1/2 states, respectively.[31,50] The absence of the satellite peaks also corroborates the assignment of the final product to Fe_3O_4 rather than Fe_2O_3.[30] This is an important character to distinguish between Fe_3O_4 (magnetite) and γ- Fe_2O_3 (maghemite) since the two have the same crystalline structure but differ only in the valence state of iron ions. The spectrum of C1s (Figure 1d) is dominated by a feature around 284.6 eV, which associates with

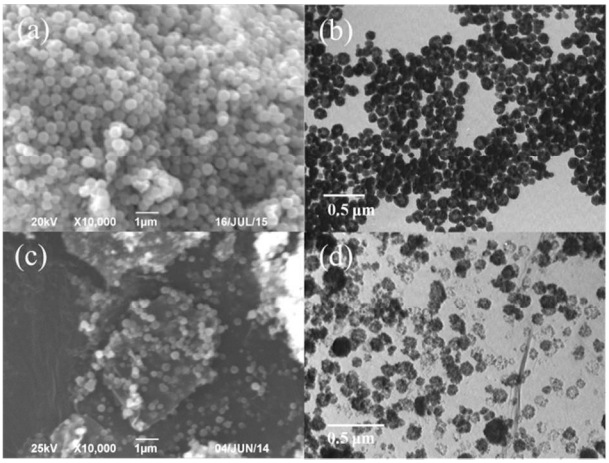

Figure 2 (a) SEM and (b) TEM images of the as prepared H-Fe_3O_4 NPs; (c) SEM and (d) TEM images of the as prepared H-Fe_3O_4/GNS nanosheets.

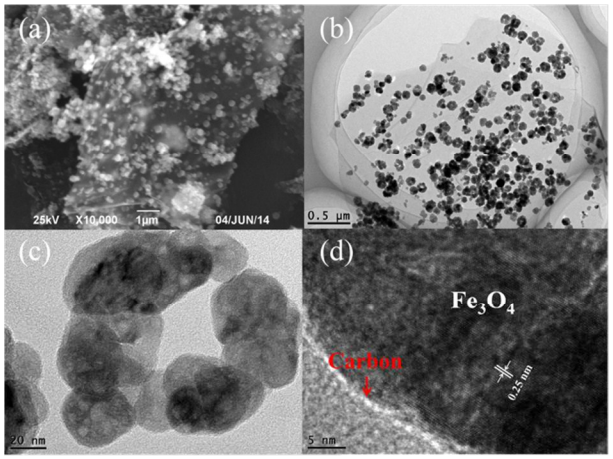

Figure 3 (a) SEM images of the as-prepared H-Fe_3O_4@C/GNS nanosheets; (b, c) TEM and (d) HRTEM images of the as-prepared H-Fe_3O_4@C/GNS nanosheets.

graphene carbon.[24] The C 1s spectra were deconvoluted into different peaks, the intensities of the peaks for all oxygen-containing functional groups strongly declined, indicative of a sufficient reduction of GO.

The morphology and microstructure of the as prepared H-Fe_3O_4NPs and H-Fe_3O_4/GNS nanosheets were characterized by scanning electron microscopy (SEM) and transmission electron microscopy (TEM) measurements. A representative SEM image of the H-Fe_3O_4NPs is shown in Figure 2a, in which the H-Fe_3O_4NPs are spherical and well-distributed. The TEM image (Figure 2b) further reveals that the H-Fe_3O_4 NPs are hollow with diameters in the range of 100-150 nm and these particles tend to be close and connected to each other. Figure 2c shows the typical SEM image of the H-Fe_3O_4@C/GNS nanosheets. It can be clearly seen that the Fe_3O_4 NPs uniformly decorated on the surface of the two-dimensional GNS, which helps to prevent the Fe_3O_4 NPs agglomerating and enables a good dispersion of Fe_3O_4 NPs over the support. The TEM image of H-Fe_3O_4/GNS nanosheets (Figure 2d) further confirms the result of SEM and reveals that the Fe_3O_4 NPs possess a hollow structure. These H-Fe_3O_4 NPs are homogeneously and firmly attached to the graphene nanosheets, even after the ultrasonication used to disperse the H-Fe_3O_4/GNS nanosheets for TEM characterization.

Figure 3 further shows the morphology and microstructure of the as prepared H-Fe_3O_4@C/GNS nanosheets by SEM and TEM. Low magnification SEM images (Figure 3a) and TEM image (Figure 3b and Figure S2 in the Supporting Information) reveal that the H-Fe_3O_4 NPs uniformly decorated on the surface of the two-dimensional GNS, which is same with that of H-Fe_3O_4/GNS nanosheets. From the higher magnification TEM image in Figure 2c, it is visible that these H-Fe_3O_4 NPs are constructed with tiny nanocrystallites in an average diameter of ca. 30 nm. From the HRTEM image in Figure 2d, the distance of the lattice fringes is around 0.25 nm, corresponding to the (311) plane of Fe_3O_4.[22,30,47] It should be emphasized that the dark Fe_3O_4 NPs are evenly covered by a light layer of amorphous carbonaceous shell with an average thickness of about 1 nm. Between the shell and the core there exists a clear interface, indicating a tight encapsulation. Therefore, we believe that such a perfect structure prevents the direct exposure of encapsulated Fe_3O_4 NPs to the electrolyte and enhances the conductivity of hybrid NPs, thus guaranteeing the efficient electrochemical performance.

The electrochemical properties of the as-synthesized H-Fe_3O_4@C/GNS nanosheets as Li-ion battery anode were investigated using a two-electrode cell with lithium metal as the counter electrode. Figure 5a shows the cyclic voltammograms (CVs) of H-Fe_3O_4@C/GNS electrode cycled between 0.05 and 3.0 V (vs Li^+/Li) at a scan rate of 0.1 mV s^{-1}. For comparison, the bare H- Fe_3O_4 NPs (Figure 5b) and H-Fe_3O_4/GNS nanosheets (Figure 5c) were also measured by using the same procedure. As shown in Figure 5(a-c), the CV curves of the three Fe_3O_4 electrodes are similar, indicating similar electrochemical reaction pathways occurred during the intercalation/de-intercalation of lithium ions. Overall, the voltages for the anodic process (at about 1.8-2.0 V) were much higher than the cathodic ones (0.5-0.8 V) on three electrodes. This large voltage difference (~1.2 V) has been attributed to the poor kinetics of the heterogeneous reactions involving three solid-state components: Fe_3O_4, Fe^0, and Li_2O.[16] Taking the CV curves of the H-Fe_3O_4@C/GNS nanosheets electrode as an example in Figure 5a, the strong reduction peak at about 0.6 V (vs Li^+/Li) is observed in the first cathodic scan, which can be attributed to the reduction of Fe^{3+} or Fe^{2+} to Fe^0 and the irreversible reaction with the electrolyte due to SEI formation.[37,42,47] In addition, a weak reduction peak at about 0.8 V (vs Li^+/Li) is also observed, which may be ascribed to be the formation of $Li_xFe_3O_4$.[47] A broad anodic peak at about 1.7 V (vs Li^+/Li) is observed in the first anodic scan, which corresponds to the reversible oxidation of Fe^0 to Fe^{2+}/Fe^{3+}.[42] In the subsequent cycles, the distinct peaks appear at 0.72 V (vs Li^+/Li) during discharge and at 1.8-1.9 V (vs Li^+/Li) during charge, exclusively corresponding to the electrochemical reduction/oxidation ($Fe_3O_4 \leftrightarrow Fe$) reactions accompanying lithium ion insertion (lithiation) and extraction (delithiation), in accord with those previously reported in the literature for Fe_3O_4-based electrodes.[8,20,47] Apparently, the peak intensity drops significantly in the second cycle, indicating the occurrence of some irreversible reactions with formation of an SEI film.[47] However, it also should be noted that there is no noticeable change of peak

intensity and integrated areas for both cathodic and anodic peaks

Cite this: DOI: 10.1039/c0xx00000x

www.rsc.org/xxxxxx

ARTICLE TYPE

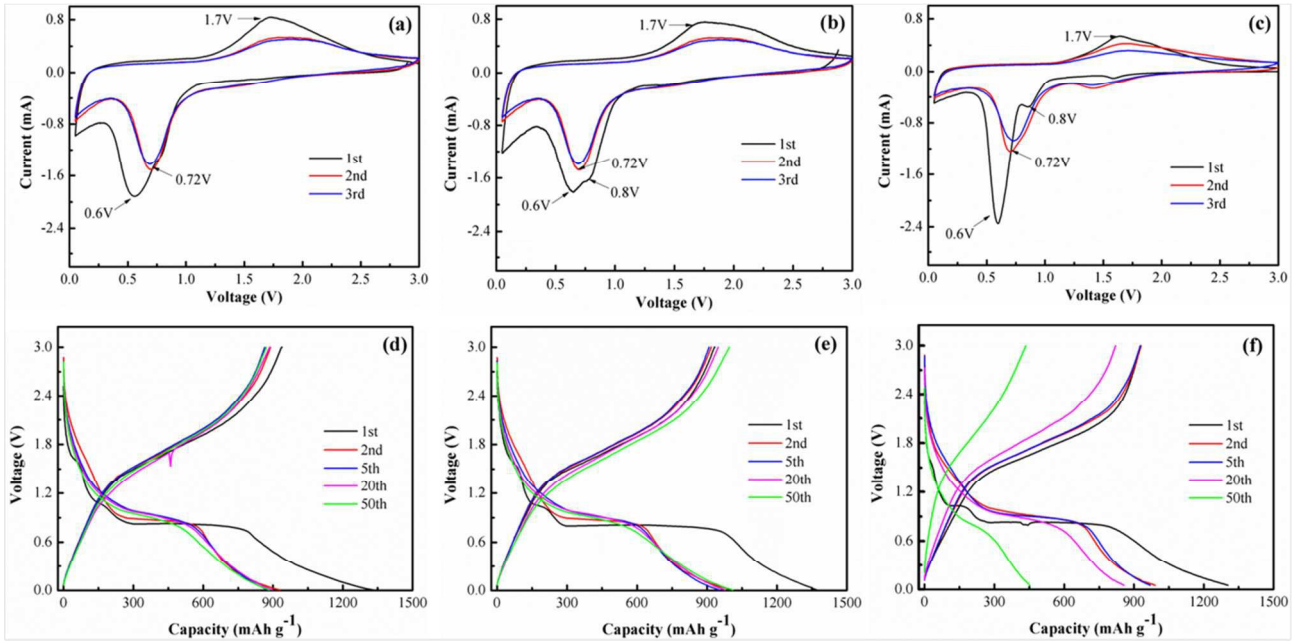

Figure 4 Cyclic voltammograms for the first three cycles of (a) H-Fe_3O_4@C/GNS nanosheets, (b) H-Fe_3O_4/GNS nanosheets and (c) H-Fe_3O_4 NPs; charge–discharge voltage profiles of (d) H-Fe_3O_4@C/GNS nanosheets, (e) H-Fe_3O_4/GNS nanosheets and (f) H-Fe_3O_4 NPs at a current density of 0.1C (1C = 1000 mA g^{-1}).

of the H-Fe_3O_4/GNS nanosheets and H-Fe_3O_4@C/GNS nanosheets after the first cycle compared with the bare H-Fe_3O_4 NPs, suggesting that the electrochemical reversibility of Fe_3O_4-graphene gradually establishes after the initial cycle and is much better than that for the bare H-Fe_3O_4 NPs.

Figure 4(d-f) compare the 1st, 2nd, 20th and 50th discharge/charge profiles of the H-Fe_3O_4@C/GNS nanosheets, H-Fe_3O_4/GNS nanosheets and H-Fe_3O_4 NPs at a current rate of 0.1C (1C = 1000 mA g^{-1}) between 0.05 and 3.0 V (vs Li^+/Li). It can be seen that the first discharge/charge voltage profiles for the three electrodes are very similar and are consistent with their corresponding CV plots. In the first discharge step, a voltage plateau can be observed at about 0.7 V (vs Li^+/Li), followed by a sloping curve down to the cut voltage of 0.05 V (vs Li^+/Li), which are typical characteristics of voltage trends for the Fe_3O_4 electrode.[5] After the first cycle, the voltage plateau became less apparent. Instead, two sloping regions at 1.6-1.0 V and 1.0-0.05 V appeared in accordance with CV profiles, indicating a different lithium reaction pathway is followed after the first complete cycle. The first specific discharge capacity of H-Fe_3O_4@C/GNS nanosheets, H-Fe_3O_4/GNS nanosheets and H-Fe_3O_4 NPs are 1331.7, 1372.8 and 1304.1 mAh g^{-1}, respectively. Compared to the theoretical capacity of bulk Fe_3O_4 (926 mAh g^{-1}) and graphene (744 mAh g^{-1}), the initial high discharge capacities of the H-Fe_3O_4@C/GNS nanosheets, H-Fe_3O_4/GNS nanosheets and H-Fe_3O_4 NPs, which have been widely observed for transition metal oxide anodes, are attributed to the formation of solid electrolyte interface (SEI) film and possibly interfacial Li^+ storage during the first discharge process,[27,29,51-53] as well as the reaction of oxygen-containing functional groups on the graphene with lithium ions.[31] It should be emphasized that an obvious change in both charge and discharge profiles is observed for the bare H-Fe_3O_4 NPs in subsequent cycles while no obvious changes are observed even after 50 cycles for H-Fe_3O_4/GNS nanosheets and H-Fe_3O_4@C/GNS nanosheets, which further indicates that the H-Fe_3O_4@C/GNS nanosheets and H-Fe_3O_4/GNS nanosheets electrodes present much better electrochemical lithium storage performance than the bare H-Fe_3O_4 NPs electrode. After five discharge/charge cycles, H-Fe_3O_4/GNS nanosheets exhibit a slowly enchanced reversible capacity (908.7 mAh g^{-1} for the 5th cycle, 948.5 mAh g^{-1} for the 20th cycle and 995.8 mAh g^{-1} for the 50th cycle) (Figure 4e). As for the H-Fe_3O_4@C/GNS nanosheets, a stable reversible capacity (~875 mAh g^{-1}) is retained up to the 50th cycle (Figure 4d). Compared to the H-Fe_3O_4@C/GNS nanosheets and H-Fe_3O_4/GNS nanosheets electrodes, the bare H-Fe_3O_4 NPs electrode shows a fast reversible capacity fading: 970 mAh g^{-1} for the 5th cycle, 857.4 mAh g^{-1} for the 20th cycle and 453.3 mAh g^{-1} for the 50th cycle (Figure 4f).

To highlight the superiority of the unique 2D H-Fe_3O_4@C/GNS nanosheets for anode materials of LIBs, Figure 5a further compare the cycle performance of the bare H-Fe_3O_4 NPs, H-Fe_3O_4/GNS nanosheets and H-Fe_3O_4@C/GNS nanosheets electrode at a current rate of 0.1C. It can be seen that the reversible capacity of the bare H-Fe_3O_4 NPs rapidly decreases from 929 to 434.7 mAh g^{-1} up to 50 cycles with only capacity retention rate of 46.8%. After anchoring H-Fe_3O_4 NPs on GNS,

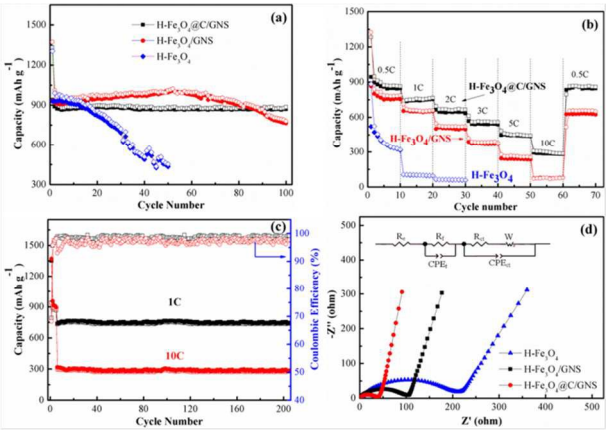

Figure 5 (a) comparative cycling performance of different electrodes at a current density of 0.1C; (b) the rate capability of H-Fe_3O_4/r-GO@C nanosheets, the H-Fe_3O_4/r-GO c nanosheets and H-Fe_3O_4 NPs at different current densities; (c) discharge/charge capacities and corresponding coulombic efficiency versus cycle number of the H-Fe_3O_4@C/GNS nanosheets electrode at rates of 1 C and 10 C for 200 cycles; (d) Nyquist plots of the H-Fe_3O_4@C/GNS nanosheets, H-Fe_3O_4/GNS nanosheets and H-Fe_3O_4 NPs after 5 cycles in the frequency range from 100 kHz to 0.01 Hz.

the specific capacity of the H-Fe_3O_4/GNS nanosheets slightly increases to about 1000 mAh g^{-1} during the initial 50 cycles, and then gradually decreased to 764.8 mAh g^{-1} after the 100th cycle, clearly indicating the beneficial effect of the GNS backbone in enhancing the capacity retention property of H-Fe_3O_4 NPs. The main reason for the gradual increased capacity of the H-Fe_3O_4/GNS electrode, which is well-documented in the literature, can be attributed to the reversible growth of a polymeric gel-like film resulting from kinetically activated electrolyte degradation.[20,22,27] However, it seems that the reversible growth of a polymeric gel-like film cannot be sustained for a long-term cycles. For comparison, the LIB performance of carbon-encapsulating H-Fe_3O_4 (H-Fe_3O_4@C) was also given in Figure S3. It can be seen that the specific capacity of the H-Fe_3O_4@C gradually decreases to 652 mAh g^{-1} after 50 cycles, indicating that there is different effect on the adding of GNS and carbon coating for improving the performance of H-Fe_3O_4. After further carbon-encapsulating H-Fe_3O_4/GNS nanosheets, the H-Fe_3O_4@C/GNS nanosheets demonstrate a better cyclic retention than that for H-Fe_3O_4/GNS nanosheets, with a high reversible capacity of 870.4 mAh g^{-1} even after 100 cycles, which is about 92.7% of the initial reversible capacity. Furthermore, its coulombic efficiency (CE) rapidly increases from 68% for the first cycle to about 98% after five cycles and remains nearly 100% in subsequent cycles, indicating that the carbon coating might be beneficial for safeguarding the structural integrity of interior Fe_3O_4 during long-term charge-discharge cycles.

It is well-known that the lithium storage capacity of Fe_3O_4 is mainly achieved through the reversible conversion reaction between the lithium ion and Fe_3O_4, forming Fe nanocrystals dispersed in Li_2O matrix.[5] Meanwhile, the Fe_3O_4-based anode surface would be covered by a SEI film during the charge/discharge process due to the reductive decomposition of the organic electrolyte.[18,19,21,47] The SEI film could rupture due to the catalyzing by the Fe nanocrystals formed during the lithium extraction processes, and thus the electrode surface would be cyclically exposed to the electrolyte, which results in continual formation of thick SEI films and accordingly continual consuming of electrolyte.[47] As a result, the cycling performance of Fe_3O_4-based anode worsen rapidly. In the case of H-Fe_3O_4@C/GNS nanosheets, the hollow structure and graphene nanosheets not only can allow for the H-Fe_3O_4 NPs to expand upon lithiation without breaking the carbon shell, but also the carbon shell can prevent the formed Fe nanocrystals from catalyzing the decomposition of the outer SEI, which allows for the growth of a stable SEI on the surface of the carbon shell and prevents the continual rupturing and re-formation of the SEI. After the formation of a stable SEI, its capacity is maintained very well and thus the anode of H-Fe_3O_4@C/GNS nanosheets exhibits exceedingly excellent cycling performance.[18,19,21]

In order to further elucidate the effect of GNS content on the electrochemical performance of the 2D H-Fe_3O_4@C/GNS nanosheets, H-Fe_3O_4@C/GNS nanosheets with different GNS content were also prepared by changing the adding amount of GO in the solvothermal process and shown in the TEM images in Figure S4. When the adding amount of GO is 150 mg (3.75 mg mL^{-1}) during the solvothermal process, the H-Fe_3O_4 NPs are few and scattered (Figure S4c). On the contrary, H-Fe_3O_4 NPs are densely and evenly distributed and anchored on graphene sheets when the adding amount of GO is 100 mg (2.5 mg mL^{-1}) (Figure S4b). However, too low adding amount of GO (50 mg, 1.25 mg mL^{-1}) should cause H-Fe_3O_4 NPs aggregation to form large clusters (Figure S4a). The cycling performance of H-Fe_3O_4@C/GNS nanosheets with different GNS content are shown in Figure S5. Although the adding amount of starting GO was adjusted from 50 mg to 150 mg, stable reversible capacity of H-Fe_3O_4@C/GNS nanosheets over 50 cycles was readily obtained from the performance testing. It is demonstrated that with increasing GO amount from from 50 mg to 150 mg, the CE of H-Fe_3O_4@C/GNS nanosheets decreased from 75% to 63.2%, which can be explained by the increase of lithium consumption on formation of SEI with increasing graphene content. Meanwhile, a high Fe_3O_4 loading results in a little degradation of reversible capacity, indicating a low utilization of Fe_3O_4 NPs in H-Fe_3O_4@C/GNS nanosheets. Thus, we can conclude that the GNS backbone can improve the utilization of Fe_3O_4 in composites apart from retaining structural integrity.

As expected, the H-Fe_3O_4@C/GNS nanosheets electrode also exhibits a significantly enhanced high rate capability, as displayed in Figure 5b. It can be clearly observed that the reversible capacity of H-Fe_3O_4@C/GNS nanosheets was kept at 845.7 mAh g^{-1} after the 10th cycle at 0.5C. Upon increasing the discharge-charge rates to 1C, 2C, 3C and 5C, the reversible capacities were maintained at about 745, 646, 540 and 445 mAh g^{-1}, respectively. Even at high rates of 10C, the reversible capacities still retain approximately 285 mAh g^{-1}. Moreover, when the current rate was finally returned to its initial value of 0.5C after a total of 60 cycles, a capacity of 850.3 mAh g^{-1} was still recoverable up to the 70th cycle. In contrast, the H-Fe_3O_4/GNS nanosheets and the bare H-Fe_3O_4 NPs show significantly lower capacity (as shown in Figure 5b), which further verifies the advantages of using the 2D H-Fe_3O_4@C/GNS nanosheets for lithium storage. Apparently, both the presence of GNS backbone and carbon nanocoating contributes to the

significantly improved electrochemical properties, in particular rate capability, of our 2D H-Fe_3O_4@C/GNS hybrid materials.

In order to further confirm the durability of H-Fe_3O_4@C/GNS nanosheets anode to work at higher rates, Figure 5c shows the discharge/charge capacities and corresponding coulombic efficiency of the H-Fe_3O_4@C/GNS nanosheets electrode at rates of 1 C and 10 C for 200 cycles. The first five cycles were first performed at 0.1 C and then 200 cycles at 1C or 10 C. It can be seen that the reversible capacities at 1C and 10 C rates are 729.8 and 295.8 mAh g^{-1}, respectively, in the initial cycle with a very slow capacity increase to 738.7 mAh g^{-1} at 1C and a very slow capacity fade to 278.7 mAh g^{-1} at 10C after 200 cycles. Such superior rate performance and cycling stability at high charge/discharge rates are significantly positive in comparison with the previous results for Fe_3O_4/carbon hybrids and other Fe-based anodes (see Table S1 in the Supporting Information), including Fe_3O_4@C nanorods (808.2 mAh g^{-1} after 100 cycles at 924 mA g^{-1}),[21] Fe_3O_4/graphene hybrids (531 mAh g^{-1} after 300 cycles at 1A g^{-1}),[26] GF@Fe_3O_4 (785 mAh g^{-1} after 500 cycles at 1C),[30] Fe_3O_4–graphene nanocomposites (180 mAh g^{-1} after 800 cycles at 10C),[40] Fe_3O_4–graphene composite (539 mAh g^{-1} after 200 cycles at 1000 mA g^{-1})[46] and even some Fe-based anodes such as mesoporous $ZnFe_2O_4$ Microrods (~524 mAh g^{-1} after 488 cycles at 1000 mA g^{-1}),[54] ZnO/$ZnFe_2O_4$@C mesoporous nanospheres (~718 mAh g^{-1} after 500 cycles at 1000 mA g^{-1}),[55] ZnO/$ZnFe_2O_4$ submicrocubes (837 mAh g^{-1} after 200 cycles at 1000 mA g^{-1}).[56] Furthermore, the CE has always been maintained over 98% at 1C and 95% at 10C during the following continuous lithiation/de-lithiation cycles, indicating its excellent reversibility for electrochemical lithium storage, which is probably due to the novel 2D carbon-encapsulated hollow nanostructure with a dual conductive network of GNS backbone and carbon nanocoating. Such a structure not only can improve the conductivity of electrodes, but also can buffer the volume expansion and contraction during the intercalation and de-intercalation process of Li ions and safeguard the structural integrity of interior Fe_3O_4 during long-term charge-discharge cycles. The SEM image of the H-Fe_3O_4@C/GNS nanosheets electrodes in the fully delithiated state after 200 discharge/charge cycles indicates that the morphology of the H-Fe_3O_4@C/GNS nanosheets still be maintained after cycling (see Supporting Information Figure S6).

In order to understand the reasons for the improved high-rate performance, electrochemical impedance spectroscopy (EIS) measurements were carried out for the bare H-Fe_3O_4 NPs, H-Fe_3O_4/GNS nanosheets and H-Fe_3O_4@C/GNS nanosheets electrodes after the 5th cycle at a current density of 0.1C, and the impedance plots along with the equivalent circuit model are presented in Figure 5d. The Nyquist plots consisted of one depressed semicircle at high frequency and an inclined line at low frequency. Generally, the semicircle is associated with the internal resistance (R_e) of the battery, the resistance (R_f) and constant phase element (CPE_f) of SEI film, the charge transfer resistance (R_{ct}) and constant phase element (CPE_{ct}) of the electrode/electrolyte interface. The inclined line represents Warburg impedance (Z_w) related to the diffusion of lithium ions within the bulk of the electrode material. The fitted impedance parameters are listed in Table S2 in the Supporting Information. The SEI film resistance R_f and charge-transfer resistance R_{ct} of the H-Fe_3O_4@C/GNS nanosheets electrode are 28Ω and 9.8Ω, which are much lower than the corresponding value of the H-Fe_3O_4/GNS nanosheets electrode (73Ω and 28.6Ω) and bare H-Fe_3O_4 NPs electrode (105Ω and 97.3Ω). This means the H-Fe_3O_4@C/GNS nanosheets have a more stable surface film and faster charge transfer process than the other samples, indicating that the presence of conductive GNS backbones and carbon shell on H-Fe_3O_4@C/GNS can greatly improve its electrical conductivity and mechanical stability, resulting in significant improvement in the electrochemical performance.

Based on above-mentioned experimental results, our 2D H-Fe_3O_4@C /GNS nanosheets display superior electrochemical performance with large reversible capacity, high rate capability, and excellent cycling performance at high rates. These outstanding properties should be attributed to their distinct structure and morphology that offer the following benefits: (1) the 2D nanosheet-type feature may ensure the short transport path for both electrons and lithium ions, leading to good conductivity and fast charge/discharge rates; (2) the thin carbon shells can prevent the encapsulated H-Fe_3O_4 nanoparticles from directly contacting with the electrolyte and alleviate the side reactions at the interface between H-Fe_3O_4 and electrolyte, resulting in structural and interfacial stabilization of H-Fe_3O_4 nanoparticles. Moreover, good electrical conductivity of the outer carbon shells can complement the low conductivity of inner H-Fe_3O_4 cores; (3) the carbon shells of the H-Fe_3O_4@C nanoparticles are interconnected through the high-conducting graphene nanosheets, thus constructing a very efficient and continuous conductive network; (4) the graphene nanosheets with excellent mechanical flexibility can efficiently inhibit the aggregation of H-Fe_3O_4 nanoparticles and circumvent the severe volume expansion/contraction of H-Fe_3O_4@C nanoparticles associated with lithium insertion/extraction and thus preserve the structural integrity of the whole electrode besides the effort contributed by the hollow structure of Fe_3O_4 nanoparticles. Due to the enhanced structural stability and integrity and excellent kinetics for lithium ion and charge transport, the lithium storage properties of our 2D H-Fe_3O_4@C /GNS nanosheets are thus remarkably improved.

4. Conclusions

In summary, novel 2D carbon-encapsulated hollow Fe_3O_4 nanoparticles anchored on gaphene nanosheets (H-Fe_3O_4@C/GNS nanosheets) have been successfully fabricated by a facile synthesis method. This unique 2D hybrid nanostructure is made of 2D graphene nanosheets on which hollow Fe_3O_4 (H-Fe_3O_4) nanoparticles coated with thin carbon shells are homogeneously anchored. In this architecture, the thin carbon shells can effectively avoid the direct exposure of encapsulated H-Fe_3O_4 to the electrolyte and preserve the structural and interfacial stabilization of H-Fe_3O_4 nanoparticles. Meanwhile, the flexible and conductive 2D GNS nanosheets and carbon shells can accommodate the mechanical stress induced by the volume change of embedded H-Fe_3O_4@C nanoparticles as well as inhibit the aggregation of H-Fe_3O_4 nanoparticles and thus maintain the structural and electrical integrity of the H-Fe_3O_4@/GNS nanosheets during the charge and discharge processes. As a result, such a 2D nanostructured electrode exhibits an extremely durable high-rate capability (738.7 mAh g^{-1} at 1 C, 278.7 mAh g^{-1}

at 10 C, after 200 cycles). Our results show that the 2D H-Fe_3O_4@/GNS nanosheets are promising anode materials for the next generation LIBs with high energy and power density.

Acknowledgements

This work was financially supported by Program for Changjiang Scholars and Innovative Research Team in University (PCSIRT, No. IRT1161), Program of Science and Technology Innovation Team in Bingtuan (No. 2011CC001), and the National Natural Science Foundation of China (No. 21263021, U1303291).

References

1 B. Dunn, H. Kamath and J. Tarascon, *Science,* 2011,334, 928-935.
2 J.B. Goodenough, *Acc. Chem. Res.,* 2013,46, 1053-1046.
3 X. Zhao, C. M. Hayner, M. C. Kung and H. H. Kung, *Adv. Energy Mater.,* 2011, 1, 1079–1084.
4 Y. Zou and Y. Wang, *ACS Nano,* 2011, 5, 8108–8114.
5 P. Poizot, S. Laruelle, S. Grugeon, L. Dupont and J. M. Tarascon, *Nature,* 2000, 407, 496–499.
6 J. S. Chen, Y. L. Cheah, Y. T. Chen, N. Jayaprakash, S. Madhavi, Y. H. Yang and X. W. Lou, *J. Phys. Chem. C,* 2009, 113 , 20504–20508
7 J. S. Chen, Y. Zhang and X. W. Lou, *ACS Appl. Mater. Interfaces,* 2011, 3, 3276–3279
8 Z. C. Yang, J. G. Shen and L. A. Archer, *J. Mater. Chem.,* 2011, 21, 11092–11097.
9 X. Wang, H. Guan, S. Chen, H. Li, T. Zhai, D. Tang, Y. Bando and D. Golberg, *Chem. Commun.,* 2011, 47, 12280–12282.
10 H. S. Kim, Y. Piao, S. H. Kang, T. Hyeon and Y. E. Sung, *Electrochem. Commun.,* 2010, 12, 382–385.
11 Y. Chen, H. Xi, L. Lu and J. Xue, *J. Mater. Chem.,* 2012, 22, 5006–5012
12 T. Muraliganth, A. V. Murugan and A. Manthiram, *Chem. Commun.,* 2009, 7360–7362.
13 K. Xie, Z. Lu, H. Huang, W. Lu, Y. Lai, J. Li, L. Zhou and Y. Liu, *J. Mater. Chem.,* 2012, 22, 5560–5567.
14 H. Guan, X. Wang, H. Li, C. Zhi, T. Zhai, Y. Bando and D. Golberg, *Chem. Commun.,* 2012, 48, 4878–4880.
15 Y. Z. Piao, H. S. Kim, Y. E. Sung, T. Hyeon, *Chem. Commun.,* 2010, 46, 118–120..
16 T. Yoon, C. Chae, Y. K. Sun, X. Zhao, H. H. Kung and J. K. Lee, *J. Mater. Chem.,* 2011, 21, 17325–17330.
17 E. Kang, Y. S. Jung, A. S. Cavanagh, G. H. Kim, S. M. George, A. C. Dillon, J. K. Kim and J. Lee, *Adv. Funct. Mater.*, 2011, 21, 2430–2438.
18 W. M. Zhang, X. L. Wu, J. S. Hu, Y. G. Guo and L. J. Wan, *Adv. Funct. Mater.,* 2008, 18, 3941–3946.
19 J. E. Lee, S. H. Yu, D. J. Lee, D. C. Lee, S. I. Han, Y. E. Sung and T. Hyeon, *Energy Environ. Sci.,* 2012, 5, 9528–9533.
20 J. X. Guo, H. F. Zhu and Y. F. Sun, *J. Mater. Chem. A,* 2015, 3, 19384-19392.
21 T. Zhu, J. S. Chen and X. W. Lou, *J. Phys. Chem. C,* 2011, 115, 9814–9820.
22 G. M. Zhou, D.-W. Wang, F. Li, L. L. Zhang, N. Li, Z.-S. Wu, L. Wen, G. Q. Lu and H.-M. Cheng, *Chem. Mater.,* 2010, 22, 5306–5313.
23 X. Dong, L. Li, C. Zhao, H.-K. Liu and Z. Guo, *J. Mater. Chem. A,* 2014, 2, 9844–9850.
24 Y. Chen, B. Song, X. Tang, L. Lu and J. Xue, *J. Mater. Chem.,* 2012, 22, 17656–17662
25 R. Wang, C. Xu, J. Sun, L. Gao and C. Lin, *J. Mater. Chem. A,* 2013, 1, 1794-1800.
26 J. S. Zhou, H. H. Song, L. L. Ma and X. H. Chen, *RSC Adv.* 2011, 1, 782–791.
27 L. Fan, B. Li, D. W. Rooney, *Chem. Commun.* 2015, 51, 1597-1600.
28 L. Li, A. Kovalchuk, H. Fei, Z. Peng, Y. Li, N. D. Kim, C. Xiang, Y. Yang, G. Ruan and J. M. Tour, *Adv. Energy Mater.,* 2015, 5, DOI:10.1002/aenm.201500171
29 B. J. Li, H. Q. Cao, J. Shao, M. Z. Qu and J. H. Warner, *J. Mater. Chem.,* 2011, 21, 5069–5075.
30 J. Luo, J. Liu, Z. Zeng, C.F. Ng, L. Ma, H. Zhang, J. Lin, Z. Shen and H.J. Fan, *Nano lett.,* 2013, 13, 6136-6143.
31 W. Wei, S. Yang, H. Zhou, I. Lieberwirth, X. Feng and K. Mullen, *Adv. Mater.,* 2013, 25, 2909-2914.
32 X. Zhu, W. Wu, Z. Liu, L. Li, J. Hu, H. Dai, L. Ding, K. Zhou, C. Wang and X. Song, *Electrochim. Acta,* 2013, 95, 24-28.
33 L. Zhuo, Y. Wu, L. Wang, J. Ming, Y. Yu, X. Zhang and F. Zhao, *J. Mater. Chem. A,* 2013, 1, 3954-3960.
34 B. J. Li, H. Q. Cao, J. Shao and M. Z. Qu, *Chem. Commun.,* 2011, 47, 10374-10376.
35 J. Zhao, B. Yang, Z. Zheng, J. Yang, Z. Yang, P. Zhang, W. Ren and X. Yan, *ACS appl. Mater. & interf.,* 2014, 6, 9890-9896.
36 J. Su, M. Cao, L. Ren and C. Hu, *J. Phy. Chem. C,* 2011, 115, 14469-14477.
37 D. Chen, G. Ji, Y. Ma, J.Y. Lee and J. Lu, *ACS appl. Mater. & interf.,* 2011, 3, 3078-3083.
38 W. W. Zhou, J. X. Zhu, C. W. Cheng, J. P. Liu, H. P. Yang, C. X. Cong, C. Guan, X. T. Jia, H. J. Fan, Q. Y. Yan, C. M. Li and T. Yu, *Energy Environ. Sci.* 2011, 4, 4954–4961.
39 Y. Z. Su, S. Li, D. Q. Wu, F. Zhang, H. W. Liang, P. F. Gao, C. Cheng and X. L. Feng, *ACS nano,* 2012, 6, 8349–8356.
40 S. K. Behera, *Chem. Commun.,* 2011, 47, 10371–10373.
41 Y. Liu, K. Huang, H. Luo, H. Li, X. Qi and J. Zhong, *RSC Adv.,* 2014, 4, 17653-17659.
42 T.-Q. Wang, X.-L. Wang, Y. Lu, Q.-Q. Xiong, X.-Y. Zhao, J.-B. Cai, S. Huang, C.-D. Gu and J.-P. Tu, *RSC Adv.,* 2014, 4, 322-330.
43 W. Chen, S. Li, C. Chen and L. Yan, *Adv. Mater.,* 2011, 23, 5679-5683.
44 X. Li, X. Huang, D. Liu, X. Wang, S. Song, L. Zhou and H. Zhang, *J. Phy. Chem. C,* 2011, 115, 21567-21573.
45 Y. Chang, J. Li, B. Wang, H. Luo, H. He, Q. Song and L. Zhi, *J. Mater. Chem. A,* 2013, 1, 14658-14665.
46 Y. Dong, R. Ma, M. Hu, H. Cheng, Q. Yang, Y.Y. Li and J. A. Zapien, *Phy. Chem. Chem. Phy.,* 2013, 15, 7174-7181.
47 C. He, S. Wu, N. Zhao, C. Shi, E. Liu and J. Li, *ACS nano,* 2013, 7, 4459-4469.
48 B. Jang, M. Park, O. B. Chae, S. Park, Y. Kim, S. M. Oh, Y. Piao and T. Hyeon, *J. Am. Chem. Soc.,* 2012, 134, 15010–15015.
49 Y. Xu, H. Bai, G. Lu, C. Li and G. Shi,, *J. Am. Chem. Soc.,* 2008, 130, 5856-5857.
50 J. Chen, J. Xu, S. Zhou, N. Zhao and C.-P. Wong, *Nano Energy* 15 (2015) 719-728.
51 Z. Y. Wang, L. Zhou and X. W. Lou, Adv. Mater., 2012, 24, 1903–1911.
52 Z. M. Cui, L. Y. Jiang, W. G. Song and Y. G. Guo, *Chem. Mater.,* 2009, 21, 1162–1166.
53 Y. Z. Su,S. Li, D. Q. Wu, F. Zhang, H. W. Liang, P. F. Gao, C. Cheng and X. L. Feng, *ACS Nano,* 2012, 6, 8349–8356.
54 L. Hou, H. Hua, L. Lian, H. Cao, S. Zhu and C. Yuan, *Chem. Eur. J.,* 2015, 21, 13012-13019.
55 C. Yan, H. Cao, S. Zhu, H. Hua and L. Hou, *J. Mater. Chem. A,* 2015,3, 20389-20398.
56 L. Hou, L. Lian, L. Zhang, G. Pang, C. Yuan and X. Zhang, *Adv. Funct. Mater.,* 2015, 25, 238-246.

A novel 2D H-Fe_3O_4@C/GNS nanosheets electrode exhibits excellent cycling stability and super high rate performance.